The Direct Estimation of Near-Bottom Turbulent Fluxes in the Presence of Energetic Wave Motions

W. J. SHAW AND J. H. TROWBRIDGE

Woods Hole Oceanographic Institution, Woods Hole, Massachusetts

(Manuscript received 20 October 1999, in final form 11 December 2000)

ABSTRACT

Velocities produced by energetic waves can contaminate direct covariance estimates of near-bottom turbulent shear stress and turbulent heat flux. A new adaptive filtering technique is introduced to minimize the contribution of wave-induced motions to measured covariances. The technique requires the use of two sensors separated in space and assumes that the spatial coherence scale of the waves is much longer than the spatial coherence scale of the turbulence. The proposed technique is applied to an extensive set of data collected in the bottom boundary layer of the New England shelf. Results from the oceanic test demonstrate that the technique succeeds at removing surface-wave contamination from shear stress and heat flux estimates using pairs of sensors separated in the vertical dimension by a distance of approximately 5 times the height of the lower sensor, even during the close passage of hurricanes. However, the technique fails at removing contamination caused by internal motions that occur occasionally in the dataset. The internal case is complicated by the facts that the motions are highly intermittent; the internal-wave period is comparable to the Reynolds-averaging period; the height of the internal-wave boundary layer is on the order of the height of measurement; and, specifically for heat flux estimates, nonlinear effects are large. The presence of internal motions does not pose a significant problem for estimating turbulent shear stress, because contamination caused by them is limited to frequencies lower than those of the stress-carrying eddies. In contrast, the presence of internal motions does pose a problem for estimating turbulent heat flux, because the contamination extends into the range of the heat flux–carrying eddies.

1. Introduction

Turbulent mixing driven by bottom drag is an essential component of shallow water flows. The dynamically significant effects of turbulence on Reynolds-averaged boundary layer flows are contained in the covariance terms that represent the vertical transport of heat and horizontal momentum (e.g., Monin and Yaglom 1971). As a result, the measurement of near-bottom, turbulence-induced shear stress and heat flux is a critical objective of coastal physical oceanography. High quality vertical flux estimates are necessary to formulate and test hypotheses regarding the dynamics of boundary layer turbulence. For example, models of currents and sediment transport on continental shelves rely heavily on how turbulent momentum flux is parameterized in the bottom boundary layer (e.g., Grant and Madsen 1986).

A number of methods are available for estimating turbulent fluxes in oceanic boundary layers. A direct vertical flux estimate is obtained by measuring the covariance between turbulent fluctuations of the transported quantity of interest (horizontal momentum or temperature) and fluctuations of vertical velocity (e.g., Bowden and Fairbairn 1956; Heathershaw 1979). Indirect methods include the profile technique (e.g., Charnock 1959; Sternberg 1968; Gross and Nowell 1983; Lueck and Lu 1997), in which fluxes are determined from the fit of semiempirical models to the vertical profiles of Reynolds-averaged quantities; the inertial-dissipation technique (e.g., Gross and Nowell 1985; Green and McCave 1995), in which fluxes are derived from Kolmogorov's theory of the inertial subrange and simplified variance budgets; and the dynamic technique (e.g., Bowden and Fairbairn 1952; Bowden et al. 1959), in which fluxes are estimated as the residual after other terms in simplified momentum or heat balances are measured. Both the profile technique and the inertial-dissipation technique rely on restrictive assumptions that often are hard to justify in the coastal ocean because of the presence of multiple length scales. In practice, the dynamic technique measures the influence of turbulence on a larger scale than the other techniques and it precludes the testing of dynamical balances.

We believe that direct measurements of turbulent fluxes will advance our understanding of the complex dynamics of the coastal bottom boundary layer. In the coastal ocean, however, direct turbulent flux measurements are often contaminated by the presence of en-

Corresponding author address: William J. Shaw, Marine Science Institute, University of California, Santa Barbara, Santa Barbara, CA 93106.
E-mail: wshaw@icess.ucsb.edu

ergetic surface (Grant et al. 1984; Grant and Madsen 1986; Huntley and Hazen 1988; Trowbridge 1998) and internal waves that are often several orders of magnitude more energetic than turbulent eddies. Slight uncertainty in estimating the principle axes of the wave-induced velocity field can dominate the turbulence-induced component of the measured covariance (see section 2).

Recently, Trowbridge (1998) introduced a novel technique for removing surface wave contamination from shear stress estimates by taking the difference of records of velocity components measured by pairs of spatially separated current meters. The technique is based on the assumption that the spatial scale of surface waves is large relative to the correlation scale of the near-bottom turbulence. Essentially, Trowbridge (1998) assumed that the wave-induced velocities at the two sensors are equal and can be canceled by subtraction.

In this paper, alternative differencing strategies are considered and a new adaptive filtering technique is introduced to reduce further wave contamination of measured covariances. The adaptive filtering technique requires wave motions at spatially separated sensors to be coherent, but not necessarily equal, allowing useful flux estimates to be made in high-energy wave conditions and permitting a wider latitude in sensor placement. Important, the technique can be applied to a vertical array of sensors, which is a practical configuration for field experiments, and the technique results in flux estimates at the locations of each of the sensors rather than a spatial average between the two sensors.

Here, methods for removing surface and internal wave-induced contributions to estimates of vertical turbulent fluxes of heat and horizontal momentum in near-bottom flows are presented. A theoretical description of, and techniques to remove, wave bias are discussed in section 2. Measurements to test the techniques are described in section 3, followed by presentation and discussion of results (sections 4 and 5), and a summary and conclusions (section 6).

2. Theoretical framework

a. Overview

A 2D model of the velocity field of the bottom boundary layer on the continental shelf, in the presence of wave motions, is developed to demonstrate wave bias and to provide a framework for the presentation of techniques for removing it. Although a simplification, a 2D analysis—in which the direction of the turbulent shear stress, the wave motions, and the components of the instrument coordinate system lie in a vertical plane—captures the important features of the wave bias problem. The 2D analysis presented here is a simplification of Trowbridge (1998), although it has been expanded to include the effects of waves on heat flux estimates and it relaxes assumptions about near-equality of wave-induced motions at the spatial scales of interest.

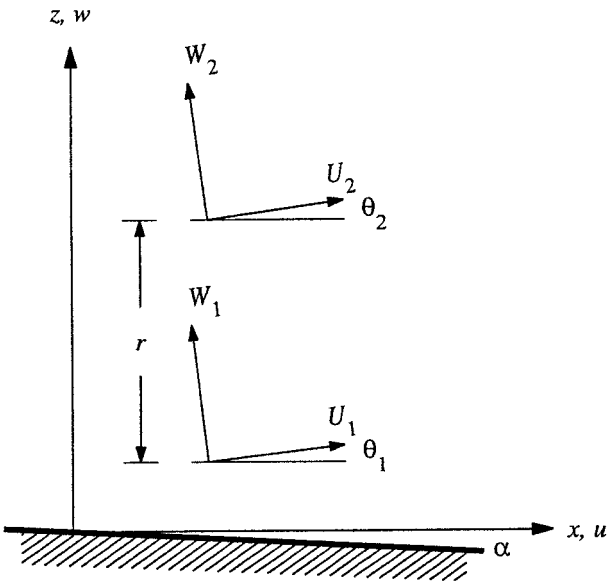

FIG. 1. Schematic diagram illustrating the geometry of the 2D bottom boundary layer model. The boundary layer is measured with two instruments whose velocity components (U_1, W_1) and (U_2, W_2) are oriented at small angles θ_1 and θ_2, respectively, to the model coordinate system (u, w). The seabed slopes at a small angle α.

The analysis relies on several assumptions. The most fundamental is that the ratio of the spatial coherence scale of the wave-induced fluctuations to the spatial coherence scale of the turbulence-induced fluctuations is large, so a spatial separation exists at which the wave-induced fluctuations are coherent and the turbulence-induced fluctuations are incoherent. We also require that the wave- and turbulence-induced fluctuations are incoherent with one another (a justifiable assumption, because waves and turbulence are essentially independent processes outside of a thin wave boundary layer), and that the statistical properties of the waves and turbulence are stationary. For the purpose of illustration, we assume that the velocity sensors have perfect response, all components of the turbulent covariance tensor have equal magnitudes [which is a good assumption for boundary layer flows (e.g., Tennekes and Lumley 1972)], the waves are of small amplitude and narrow-banded in frequency, and stratification is due to a uniform vertical temperature gradient.

The horizontal component x of the model position vector $\mathbf{x} = (x, z)$ lies in the common direction of the wave propagation and the shear stress, and the vertical component z is defined to be positive upward with $z = 0$ at the bed (Fig. 1). The model velocity vector $\mathbf{u} = (u, w)$ where u and w are the horizontal and vertical components of the velocity, respectively, is composed of contributions from, respectively, mean current, waves, and turbulence: $\mathbf{u} = \overline{\mathbf{u}} + \tilde{\mathbf{u}} + \mathbf{u}'$. The temperature similarly is denoted by $T = \overline{T} + \tilde{T} + T'$. The wave-induced component of the fluctuations can include contributions from both surface and internal waves, al-

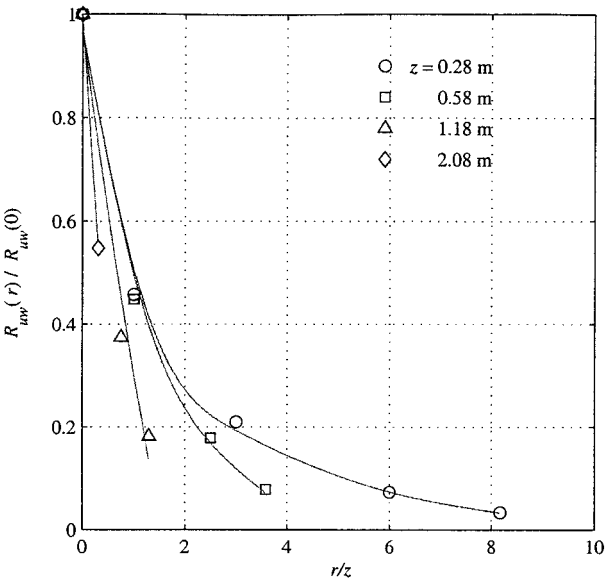

FIG. 2. Estimates of the normalized cross-correlation function $R_{uw}(r)/R_{uw}(0)$, where $R_{uw}(r) = \overline{u(z)w(z + r)}$, for positive vertical separations r estimated from measurements obtained in the Hudson River estuary at four heights above the bottom. Each curve represents an average derived from 720 3.28-min bursts of data.

though we do not consider interactions between them. The quantities of interest are the turbulent shear stress $-\rho\overline{u'w'}$ and the turbulent vertical heat flux $\rho c_p\overline{T'w'}$, where ρ is density and c_p is heat capacity.

In the remainder of this section, we first illustrate the problem of wave bias that results from a simple application of the direct eddy correlation technique to measurements obtained with an instrument that is tilted with respect to the principle axes of energetic surface wave motions (section 2b). We demonstrate that taking the difference of records from spatially separated sensors can be used to reduce the wave bias (section 2c). Then, in contrast to the previous estimates that assume the wave motions are essentially equal at the two positions, we introduce a linear filtering technique that further reduces wave bias by accounting for small differences in wave amplitude or phase between the two sensors (section 2d). Finally, we present an empirical constraint on the magnitude of the vertical separations that satisfies the critical assumption that the turbulent fluctuations at the two locations be uncorrelated (section 2e).

b. The wave bias problem

An estimate of $\overline{u'w'}$ using the velocity $\mathbf{U} = (U, W)$, measured in instrument coordinates that are rotated a small angle θ from the model coordinate system (Fig. 1) to first order in θ, is

$$\mathrm{cov}(U, W) = \overline{u'w'} + \overline{\tilde{u}\tilde{w}} + \theta[(\overline{w'^2} - \overline{u'^2}) + (\overline{\tilde{w}^2} - \overline{\tilde{u}^2})]. \quad (1)$$

In a similar way, an estimate of $\overline{T'w'}$ to first order in θ is

$$\mathrm{cov}(T, W) = \overline{T'w'} + \overline{\tilde{T}\tilde{w}} + \theta(\overline{T'u'} + \overline{\tilde{T}\tilde{u}}). \quad (2)$$

The first term on the right side of (1) and (2) is the desired vertical turbulent flux of horizontal momentum or heat, respectively. The second term is a ''real'' wave bias, representing vertical transport by waves. The third and fourth terms are ''apparent'' turbulence- and wave-induced biases arising from the orientation of the instrument coordinate system. The apparent turbulence bias is the well-known instrument leveling error (Pond 1968).

For the case of gentle bottom slopes, small rotation angles, and irrotational waves, the turbulence bias in (1) is small, but the wave biases can be an order of magnitude larger than the desired turbulent momentum flux (Trowbridge 1998). Observations in the atmospheric boundary layer indicate that the components of the heat flux vector have the same order of magnitude (Kaimal et al. 1972), indicating that the turbulence bias in (2) is small in comparison with the desired covariance if θ is small. We can estimate the real wave bias in (2) as follows. For the case of a uniform vertical temperature gradient and small-amplitude motions, the wave-induced temperature fluctuations arise from advection of the vertical temperature gradient and, for progressive waves, may be estimated as

$$\tilde{T} = -z\frac{d\overline{T}}{dz}\frac{\tilde{u}}{c}, \quad (3)$$

where c is the wave phase speed. $\overline{T'w'}$ may be estimated roughly as $-\kappa z u_* d\overline{T}/dz$ (e.g., Businger et al. 1971), where u_* is the bottom friction velocity and κ (=0.4) is von Kármán's constant. With these estimates, the ratio of wave-induced bias to turbulent heat flux is

$$\frac{\overline{\tilde{T}\tilde{w}}}{\overline{T'w'}} = O\left(\frac{\theta\overline{\tilde{T}\tilde{u}}}{\overline{T'w'}}\right) = O\left(\frac{\theta\overline{\tilde{u}^2}}{u_* c}\right), \quad (4)$$

indicating that for near-bottom values typical of the outer shelf for surface waves ($\overline{\tilde{u}^2} = 0.01\ \mathrm{m^2\ s^{-2}}$, $c = 20\ \mathrm{m\ s^{-1}}$, $u_* = 0.01\ \mathrm{m\ s^{-1}}$, and $\theta = 0.01$), the wave-induced bias is 3 orders of magnitude smaller than the turbulent heat flux.

If the measured velocity vector can be rotated into the principal axes of the wave-induced velocity field, the wave biases are removed. In practice, the orientation of the principal coordinates of the wave-induced velocity field usually is not known with sufficient accuracy to remove wave bias by rotation. The objective of the present analysis is thus to consider alternative techniques for removing the real and apparent wave biases from estimates of the turbulent covariances $\overline{u'w'}$ and $\overline{T'w'}$ in (1) and (2).

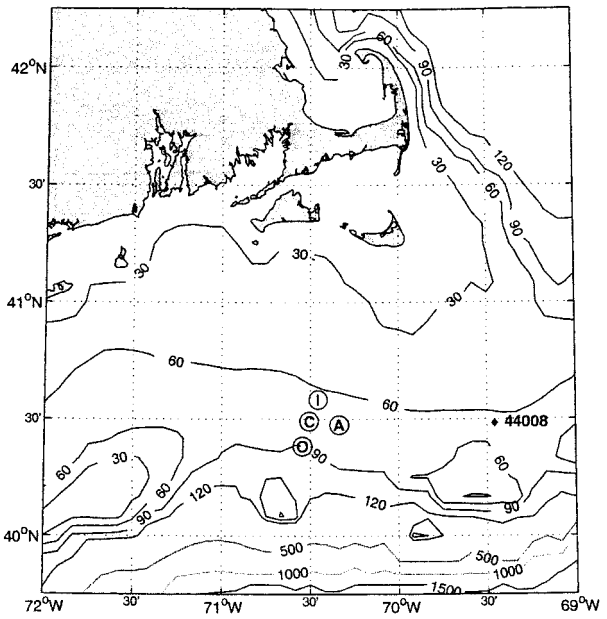

FIG. 3. Map of the CMO experiment site. Water depth is contoured in meters. The site is approximately 100 km south of Martha's Vineyard, MA, on a portion of the New England shelf known as the ''Mud Patch.'' Along with the bottom tripod, an array of four moorings were deployed. The tripod was within 200 m of the central mooring (C), in 70 m of water. Here, I, O, and A represent the locations of onshore, offshore, and alongshore moorings, respectively. [Reproduced from Fredericks et al. (1999).]

c. *Differencing strategies*

Trowbridge (1998) showed that the wave bias in estimates of momentum flux can be reduced to an acceptable level by taking the difference of (''differencing'') measurements obtained from two sensors separated by a distance large in comparison with the correlation scale of the turbulence but small in comparison with the inverse wavenumber of the waves, assuming that the correlation scale of the waves is much greater than the correlation scale of the turbulence and that the waves and turbulence are uncorrelated. Here, a slightly different approach in which only one of the measurements composing the covariance is differenced, is used. This approach is beneficial because the resulting covariance estimate corresponds to the position of a single sensor, rather than an average of the covariances at each sensor, and two estimates are available for each sensor. The resulting turbulence estimates are not independent, but the waves are removed with essentially independent information, so the redundant estimates provide a check on the technique.

In the following, a parenthesized subscript is used to identify the position at which a particular measurement is obtained. For example, $u_{(1)}$ is the horizontal velocity measured at the location of the first sensor. The operations of differencing and averaging between two sensors are represented by an upper-case delta sign and angular brackets, respectively. For example, Δu and $\langle u \rangle$ are the difference and average, respectively, of the horizontal velocities measured by a pair of sensors. We focus here on the differencing of velocity measurements.

We consider three estimates of $\overline{u'w'}$ given measurements at a pair of sensors: (1/2)cov(ΔU, ΔW), cov[ΔU, $W_{(1)}$], and cov[$U_{(1)}$, ΔW]. The assumption that wave- and turbulence-induced velocities are uncorrelated (justified in section 2a), immediately allows us to decompose contributions to the $\overline{u'w'}$ estimates into turbulence and wave components.

Assuming the turbulent fluctuations are uncorrelated at the two locations (discussed further in Section 2e), the turbulent component of the three estimates of $\overline{u'w'}$ can be written (to first order in the small angles θ_1 and θ_2; see Fig. 1) as

$$(1/2)\,\mathrm{cov}(\Delta U', \Delta W') = \langle \overline{u'w'} \rangle + \langle \theta(\overline{w'^2} - \overline{u'^2}) \rangle, \quad (5)$$

$$\mathrm{cov}[\Delta U', W'_{(1)}] = \overline{u'_{(1)}w'_{(1)}} + \theta_{(1)}[\overline{w'^2_{(1)}} - \overline{u'^2_{(1)}}], \quad (6)$$

and

$$\mathrm{cov}[U'_{(1)}, \Delta W'] = \overline{u'_{(1)}w'_{(1)}} + \theta_{(1)}[\overline{w'^2_{(1)}} - \overline{u'^2_{(1)}}]. \quad (7)$$

The first term on the right side of (5) is an average of the turbulence-induced covariance at each of the sensors, and the first term on the right side of (6) and (7) is the desired turbulence-induced covariance at the location of the first sensor. The second term on the right side of (5)–(7) is a small apparent turbulence bias.

The wave component of the three $\overline{u'w'}$ estimates may be written (also to first order in θ_1 and θ_2) as

$$\begin{aligned}(1/2)\,\mathrm{cov}(\Delta\tilde{U}, \Delta\tilde{W}) &= (1/2)\overline{\Delta\tilde{u}\Delta\tilde{w}} \\ &\quad + (1/2)\langle\theta\rangle(\overline{\Delta\tilde{w}^2} - \overline{\Delta\tilde{u}^2}) \\ &\quad + (1/4)\Delta\theta(\Delta\overline{\tilde{w}^2} - \Delta\overline{\tilde{u}^2}), \quad (8)\end{aligned}$$

$$\begin{aligned}\mathrm{cov}[\Delta\tilde{U}, \tilde{W}_{(1)}] &= \overline{\tilde{w}_{(1)}\Delta\tilde{u}} + \theta_{(1)}[\overline{\tilde{w}_{(1)}\Delta\tilde{w}} - \overline{\tilde{u}_{(1)}\Delta\tilde{u}}] \\ &\quad + \Delta\theta[\overline{\tilde{w}^2_{(1)}} - \overline{\tilde{w}_{(1)}\Delta\tilde{w}}], \quad (9)\end{aligned}$$

and

$$\begin{aligned}\mathrm{cov}[\tilde{U}_{(1)}, \Delta\tilde{W}] &= \overline{\tilde{u}_{(1)}\Delta\tilde{w}} + \theta_{(1)}[\overline{\tilde{w}_{(1)}\Delta\tilde{w}} - \overline{\tilde{u}_{(1)}\Delta\tilde{u}}] \\ &\quad - \Delta\theta[\overline{\tilde{u}^2_{(1)}} - \overline{\tilde{u}_{(1)}\Delta\tilde{u}}]. \quad (10)\end{aligned}$$

Wave contributions to the measured covariance arise from differences in wave-induced velocity between the two locations and differences in alignment between the two sensors. We note that, in contrast to (5)–(7), (8)–(10) contain correlation terms between the two positions and that the differencing techniques, in principle, would work perfectly if the wave-induced fluctuations at the two locations were equal. There obviously is a compromise in choosing the separation distance between having the turbulence uncorrelated and the waves highly correlated.

To illustrate the magnitudes of the terms in (8)–(10), we restrict the scope of the analysis to the measurement of turbulence in the presence of surface waves with a pair of vertically separated sensors. Differenced quan-

tities are represented with first-order expansions. For example, $\Delta u \simeq r\partial\tilde{u}/\partial z$, where r is the separation between the sensors and $\partial\tilde{u}/\partial z$ is evaluated at a location between the two sensors for the estimate (1/2)cov($\Delta\tilde{U}$, $\Delta\tilde{W}$) and at the location of the first sensor for the estimates cov[ΔU, $W_{(1)}$] and cov[$U_{(1)}$, ΔW]. Also, we assume that $kz \ll 1$, where k is the wavenumber of the waves, allowing the hyperbolic functions describing the vertical variation of wave-induced velocity to be represented with first-order expansions. With these assumptions, (8)–(10) can be approximated as

$$(1/2)\ \mathrm{cov}(\Delta\tilde{U},\ \Delta\tilde{W}) \simeq (r^2/2z^2)[k^2z^2\langle\overline{\tilde{u}\tilde{w}}\rangle + \langle\theta\rangle(\langle\overline{\tilde{w}^2}\rangle - k^4z^4\langle\overline{\tilde{w}^2}\rangle) + \Delta\theta(\langle\overline{\tilde{w}^2}\rangle - k^4z^4\langle\overline{\tilde{u}^2}\rangle)], \quad (11)$$

$$\mathrm{cov}[\Delta\tilde{U},\ \tilde{W}_{(1)}] \simeq (r/z)\left\{k^2z^2\overline{\tilde{u}_{(1)}\tilde{w}_{(1)}} + \theta_{(1)}[\overline{\tilde{w}^2_{(1)}} - k^2z^2\overline{\tilde{u}^2_{(1)}}] + \Delta\theta\overline{\tilde{w}^2_{(1)}}\left(\frac{z}{r}+1\right)\right\}, \quad \text{and} \quad (12)$$

$$\mathrm{cov}[\tilde{U}_{(1)},\ \Delta\tilde{W}] \simeq (r/z)\left\{\overline{\tilde{u}_{(1)}\tilde{w}_{(1)}} + \theta_{(1)}[\overline{\tilde{w}^2_{(1)}} - k^2z^2\overline{\tilde{u}^2_{(1)}}] - \Delta\theta\overline{\tilde{u}^2_{(1)}}\left(k^2z^2+\frac{z}{r}\right)\right\}. \quad (13)$$

For near-bottom measurements, we expect that terms like $\overline{\tilde{u}\tilde{w}}$, $\theta\overline{\tilde{u}^2}$, and $\Delta\theta\overline{\tilde{u}^2}$ are of comparable magnitude and much larger than terms such as $\theta\overline{\tilde{w}^2}$ and $\Delta\theta\overline{\tilde{w}^2}$. All of the large terms on the right side of (11) and (12) have been reduced by at least the factor k^2rz, while two of the large terms in (13) have only been reduced by the factor r/z, which is constrained by the assumption that the turbulence must be uncorrelated at the two positions to be of order 1 (see section 2e). The stress estimate (1/2)cov($\Delta\tilde{U}$, $\Delta\tilde{W}$) has a greater reduction in wave bias at the cost of averaging the turbulent covariances between the two locations. For near-bottom measurements, the reduction in apparent wave bias resulting from the rotation of horizontal velocity into the vertical is better for (1/2)cov($\Delta\tilde{U}$, $\Delta\tilde{W}$) by an additional factor of k^2rz.

d. Further reduction in wave bias with adaptive filtering

Failure of the differencing technique described in section 2c occurs under conditions of high wave energy if differences in amplitude or phase of the wave-induced motions between the two locations cause the difference terms $\Delta\tilde{u}$ or $\Delta\tilde{w}$ appearing in (8)–(10) to be significant. A solution is to minimize the difference terms with linear filtration techniques. Assuming that the wave-induced fluctuations are completely spatially coherent, least squares filtering can be used to estimate the coherent component of velocity at one position with velocity measurements at the second position. Thus, the assumption behind the simple differencing technique used earlier—that the wave-induced motions at the two sensors are essentially identical—is replaced by the assumption that the wave-induced motions at the two sensors are essentially perfectly coherent. This relaxation allows potential differences in wave phase and amplitude that contribute to the difference terms in (8)–(10) to be minimized. In other words, because the coherence scale of wave motions is expected to be greater than the correlation scale, the filtering technique extends the range of application of the differencing techniques. The assumption that the turbulence is spatially uncorrelated is replaced by the assumption that the turbulence is spatially incoherent.

Here, the analysis is no longer limited to vertical separations. We begin by using the assumption that the wave motions at the two positions are coherent to establish a linear functional relationship between the wave-induced fluctuations measured at positions (1) and

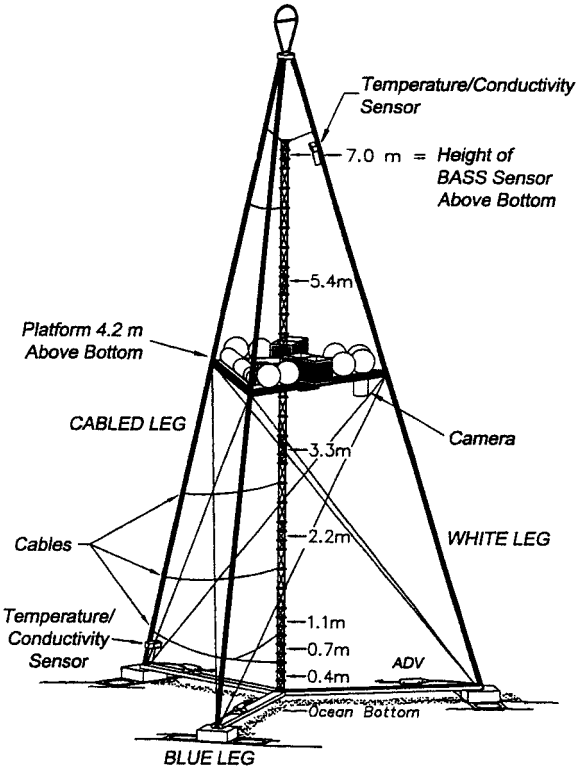

FIG. 4. Scale drawing of the ''SuperBASS'' tripod deployed as a part of the CMO experiment. The tripod was 8 m tall, containing a vertical array of BASS current meters, a horizontal array of acoustic Doppler velocimeters, and a pair of temperature and conductivity sensors. The heights of the BASS sensors above the bottom are marked. [Reproduced from Fredericks et al. (1999).]

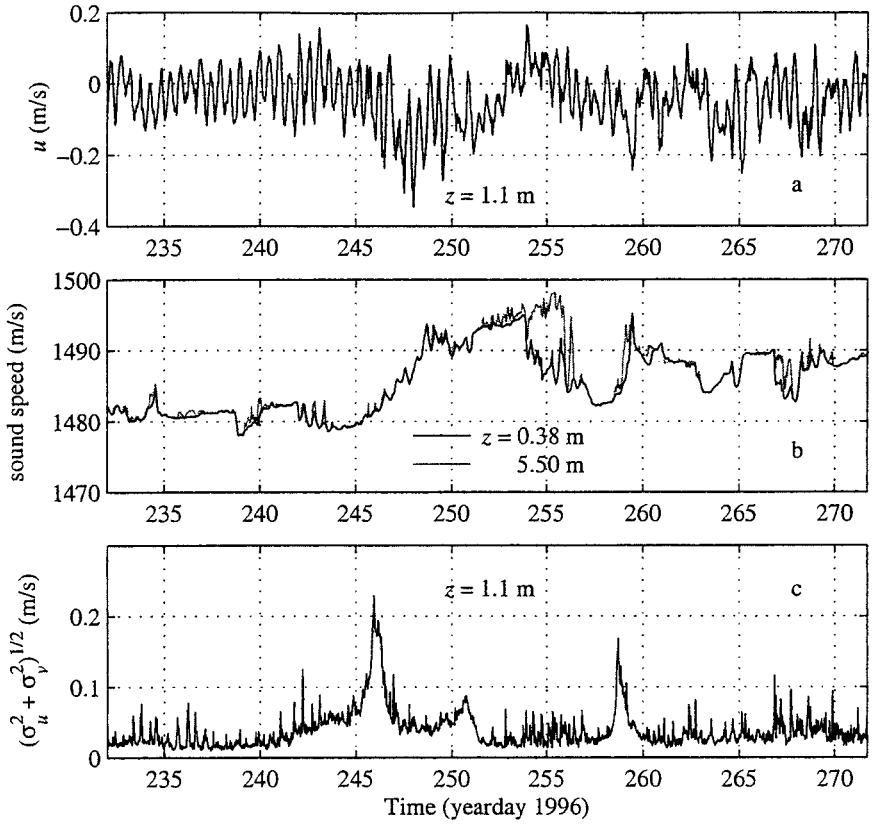

FIG. 5. Time series of (a) burst-averaged, along-shelf current, (b) burst-averaged sound speed, and (c) burst standard deviations of horizontal velocity $\sqrt{\sigma_u^2 + \sigma_v^2}$ measured by the BASS array. Statistics are from 27-min bursts. The coordinate system is oriented so that eastward flow is positive.

(2). For example, the wave-induced horizontal velocities are assumed to be related by

$$\tilde{U}_{(1)}(t) = \int_{-\infty}^{\infty} h(t')\tilde{U}_{(2)}(t - t')\, dt'. \qquad (14)$$

Here, t is time and $h(t)$ is a filter that represents the relationship between the wave-induced fluctuations at the two locations. In effect, (14) states that if $\tilde{U}_{(1)}$ and $\tilde{U}_{(2)}$ are perfectly coherent, then $\tilde{U}_{(1)}$ is completely predictable from $\tilde{U}_{(2)}$. The goal of this analysis is to use the total measured velocities to estimate $h(t)$. A more nearly wave-free estimate of horizontal velocity at position (1) than $\Delta U = U_{(1)} - U_{(2)}$ is then $\Delta\hat{U} = U_{(1)} - \hat{U}_{(1)}$, where

$$\hat{U}_{(1)}(t) = \int_{-\infty}^{\infty} \hat{h}(t')U_{(2)}(t - t')\, dt' \qquad (15)$$

is the estimated wave-induced velocity at position (1), using estimates of the filter weights $\hat{h}(t)$ and the measured velocities at position (2). The estimated wave velocity $\hat{U}_{(1)}$ contains a turbulence component, but it is of no consequence if the assumption that the turbulence is spatially incoherent is valid. If the estimates cov[ΔU, $W_{(1)}$] and cov[$U_{(1)}$, ΔW] are replaced by cov[$\Delta\hat{U}$, $W_{(1)}$] and cov[$U_{(1)}$, $\Delta\hat{W}$], respectively, the problematic difference terms appearing in (9) and (10) are minimized to the extent that the model assumptions are valid.

The filter weights in (14) are estimated by finding the ordinary least squares solution of a transversal filter model (e.g., Haykin 1996) that has been modified to a noncausal form for postprocessing purposes:

$$\mathbf{A}h = U_{(1)}. \qquad (16)$$

Here, $\mathbf{A}$ is an $M \times N$ windowed data matrix of velocity at position (2), where M is the number of data points and N is the number of filter weights (N must be odd for the filter to be symmetric), $\mathbf{h}$ is a vector of filter weights, and $\mathbf{U}_{(1)}$ is a vector of position (1) velocity. The mth row of $\mathbf{A}$ is [$u(m - (N - 1)/2), \ldots, u(m), \ldots, u(m + (N - 1)/2)$], where $u(m)$ is the mth discrete sample of u. The solution is

$$\hat{\mathbf{h}} = (\mathbf{A}^T\mathbf{A})^{-1}\mathbf{A}^T\mathbf{U}_{(1)}, \qquad (17)$$

and estimates $\hat{\mathbf{U}}_{(1)}$ of the wave-induced velocity at position (1) are found by convolving the measured velocity record with the estimated filter weights

$$\hat{\mathbf{U}}_{(1)} = \mathbf{A}\hat{\mathbf{h}}. \qquad (18)$$

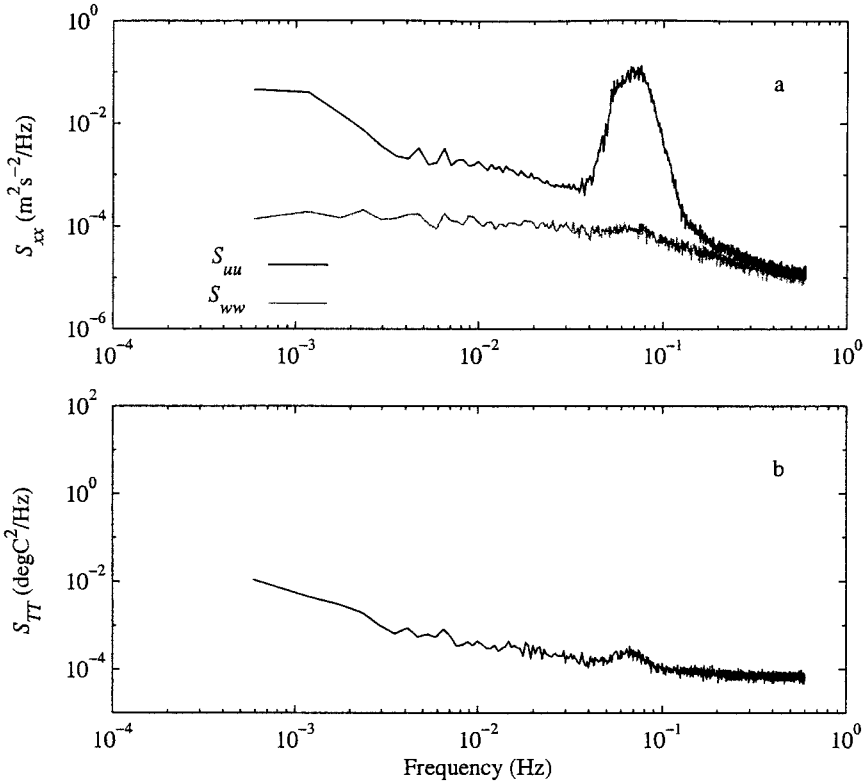

FIG. 6. Energy density spectra of (a) longitudinal and vertical velocity fluctuations and (b) temperature fluctuations from BASS measurements at 0.70 m above the bed when energetic surface waves were present. The spectral densities are average values from 49 bursts when the rms horizontal surface-wave velocity in the frequency band 0.04 Hz $\leq f \leq$ 0.2 Hz was greater than 0.04 m s^{-1}.

In practice, we have encountered some complications in applying the filtering technique described above (to be discussed below); in general, however, robust estimates of the filter weights are obtainable with the adjustment of only two significant parameters: the number of data points M and the number of filter weights N.

e. Turbulence correlation lengths

For these wave bias removal techniques to work in practice, the sensor separation must be large relative to the correlation length scale of the turbulence so that the turbulence cross-correlation terms $\overline{u'_{(1)}u'_{(2)}}$, $\overline{u'_{(1)}w'_{(2)}}$, $\overline{w'_{(1)}u'_{(2)}}$ neglected in (5)–(7) (by the assumption that the turbulent fluctuations at the two positions are uncorrelated) are small. It is easily shown that all of the cross correlation terms except $\overline{u'_{(1)}w'_{(2)}}$ are multiplied by θ, and therefore, assuming that the elements of the turbulent correlation function tensor have the same order of magnitude, we only need to ensure that $\overline{u'_{(1)}w'_{(2)}}$ is small as compared with $\overline{u'_{(1)}w'_{(1)}}$. Because of the strong intermittency of turbulent eddies, we expect that the turbulent coherency scale is nearly equal to the turbulent correlation scale.

We have established an empirical guideline ensuring that $\overline{u'_{(1)}w'_{(2)}}$ is small by considering the off-diagonal component of the turbulent correlation function tensor obtained in an estuarine bottom boundary layer. Trowbridge et al. (1999) reported the deployment in August of 1995 of a quadrapod on the bed of the Hudson River adjacent to Manhattan, New York, for two weeks with a vertical array of five Benthic Acoustic Stress Sensor (BASS) current meters (see section 3) at heights of 0.3, 0.6, 1.2, 2.1, and 2.4 m above the bottom in a wave-free turbulent boundary layer. The instruments were sampled in bursts of 3.28 min at 6.25 Hz. To evaluate the importance of $\overline{u'_{(1)}w'_{(2)}}$, we calculated representative cross-correlation functions by taking the average over a period of five days of $R_{uw} = \overline{u(z)w(z + r)}$ calculated from the 3.28-min bursts of data (Fig. 2). The cross-correlation functions indicate that the ratio of the vertical separation to the height of the lower sensor r/z must be greater than approximately 5 for the turbulence to be considered uncorrelated, that is, less than one-tenth of the value at zero separation. In this particular environment, the cross-correlation function decreases more rapidly as z increases, possibly because the scale of the eddies is limited by factors other than height above bottom (Trowbridge et al. 1999).

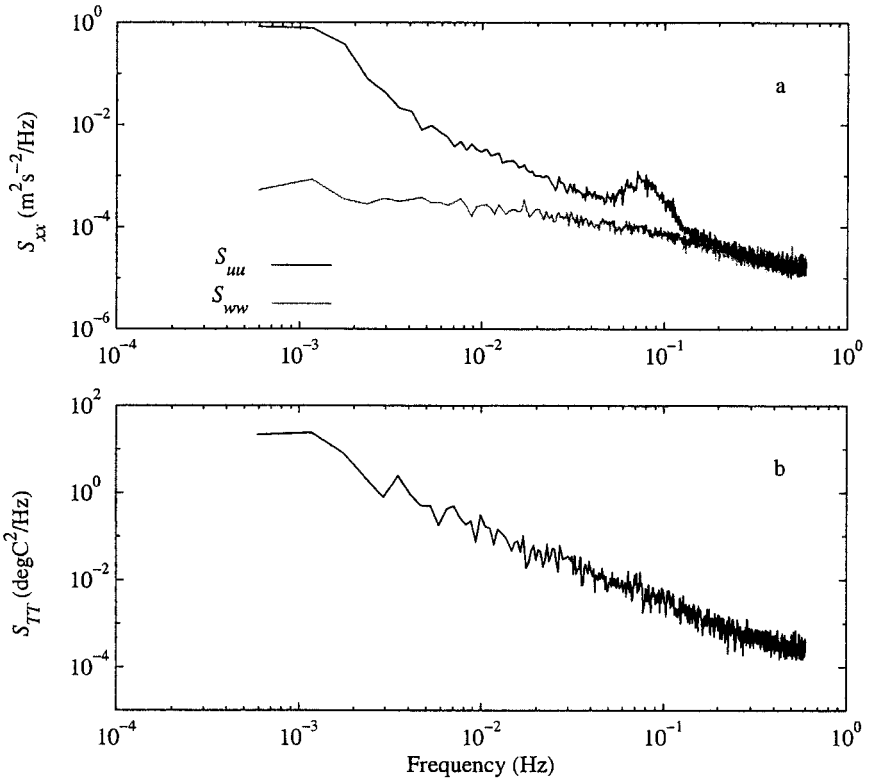

FIG. 7. Energy density spectra of (a) longitudinal and vertical velocity fluctuation and (b) temperature fluctuations from BASS measurements at 0.70 m above the bed when energetic internal waves were present. The spectral densities are average values from 49 bursts when the rms horizontal velocity minus the rms surface wave velocity was greater than 0.025 m s^{-1}.

3. Measurements and analysis

The techniques described in section 2 are tested on a set of measurements collected as part of the Coastal Mixing and Optics (CMO) experiment during 1996–97. One component of the field experiment consisted of the deployment of a bottom tripod equipped with current meters to study the turbulence dynamics of the coastal bottom boundary layer. The techniques are applied to vertically separated pairs roughly satisfying the empirical constraint $r/z > 5$ discussed in section 2c. Three sets of turbulent shear stress and vertical heat flux estimates were made: raw covariance, covariance with differencing, and covariance with differencing and adaptive filtering.

For the purposes of this paper, we limit our attention to a 6-week deployment of the bottom tripod, which began 17 August 1996. The tripod was deployed at a depth of 70 m on the New England shelf (Fig. 3). The ''SuperBASS'' tripod deployed during the CMO experiment (Fredericks et al. 1999) was outfitted with a vertical array of seven BASS current meters (Williams et al. 1987), a horizontal array of acoustic Doppler velocimeters, and a pair of temperature and conductivity sensors (Fig. 4). The BASS sensor measures the three-dimensional velocity vector by determining the differential travel time of acoustic pulses traveling in opposite directions along four 15-cm acoustic axes. The BASS electronics were modified recently to measure the absolute travel time of acoustic pulses (Trivett 1991; Shaw et al. 1996), allowing the measurement of sound speed in addition to fluid velocity. The vertical BASS array consisted of seven sensors at heights of 0.4, 0.7, 1.1, 2.2, 3.3, 5.4, and 7.0 m above the bed. The sensors were sampled at 1.2 Hz in 27-min bursts for a total of 2060 samples per burst. The bursts were taken in 2-h cycles consisting of three 0.5-h periods, during which the instruments were sampled, followed by one 0.5-h period, during which the instruments were idle.

Velocity and sound-speed measurements from the BASS array were used to produce estimates of turbulent shear stress and vertical heat flux at the lower six measurement levels. Sound-speed fluctuations were converted to temperature fluctuations by assuming a linear relationship, $\partial T/\partial c_s = 0.5°\text{C m}^{-1}\text{ s}^{-1}$, where c_s is the speed of sound, estimated from the equation of state (MacKenzie 1981) at a reference salinity of 32 psu, which is the average salinity during the deployment. All flux estimates were derived from individual 27-min bursts of 1.2-Hz data. Approximately satisfying the empirical constraint $r > 5z$, the sensors were paired for

the purposes of differencing as follows: 0.38 and 2.20 m, 0.74 and 3.30 m, and 1.10 and 5.40 m.

To test the techniques described in section 2, we computed three sets of $\overline{u'w'}$ estimates in an order of increasing sophistication to remove wave contamination: a ''raw'' estimate, cov(U, W); two ''differenced'' estimates, cov(ΔU, W) and cov(U, ΔW); and two ''filtered'' estimates, cov($\Delta \hat{U}$, W) and cov(U, $\Delta \hat{W}$). An analogous set of $\overline{T'w'}$ covariances was also computed. Flux estimates were obtained by integrating the cospectrum of $u(t)$ and $w(t)$, denoted Co_{uw}, and the cospectrum of $T(t)$ and $w(t)$, denoted Co_{Tw}. All spectral and cospectral calculations were carried out in a coordinate system aligned with the burst-averaged flow and resulting shear stress estimates were then rotated into a coordinate system oriented in the along- and cross-shelf directions.

For the filtered estimates, we obtained wave-induced velocity records with an expanded form of the transversal filter model (16) in which all three components of velocity measured at the second sensor were used as inputs, resulting in an $M \times 3N$ data matrix $\mathbf{A}$. The mth row of the expanded data matrix $\mathbf{A}$ is

$$\left[u\left(m - \frac{N-1}{2}\right), \ldots, u(m), \ldots, u\left(m + \frac{N-1}{2}\right), v\left(m - \frac{N-1}{2}\right), \ldots, v(m), \ldots, v\left(m + \frac{N-1}{2}\right), w\left(m - \frac{N-1}{2}\right), \ldots, w(m), \ldots, w\left(m + \frac{N-1}{2}\right)\right],$$

where $u(m)$, $v(m)$, and $w(m)$ are the mth discrete sample components of the velocity vector $\mathbf{u}$.

Including all three velocity components in $\mathbf{A}$ increases the number of degrees of freedom by approximately a factor of 3. Filtered temperature records were obtained by applying the original model (16) directly, with T replacing U. The filter weights were calculated with (17) and applied to the measured data according to (18). The length of the filter was $N = 11$, corresponding to a window length of 9.2 s, which is about one-half of the typical wave period at the CMO site, and resulted in a total of 33 filter weights for each estimated component of wave-induced velocity fluctuations, and 11 filter weights for estimated wave-induced temperature fluctuations. New filters were calculated for each burst, so the filtering technique was block adaptive to slowly changing wave conditions. As a result, there were $3M - 3N = 6447$ degrees of freedom in the velocity regression and $M - N = 2049$ degrees of freedom in the temperature regression.

4. Results

a. Conditions at the CMO site

Before proceeding to a test of the proposed techniques for removing wave bias, it is worthwhile to briefly describe the conditions at the CMO field site during the first deployment. Here, we describe the temporal variability of burst statistics and we present spectra representative of conditions of energetic surface waves and conditions of energetic internal motions.

Time series of near-bottom mean currents at the CMO site (Fig. 5a) are usually dominated by a rotary semidiurnal tide with an amplitude of approximately 0.1 m s^{-1}. Subtidal events consist of predominantly westward flows with velocities up to 0.2 m s^{-1}. Time series of mean sound speed measured by the top and bottom BASS sensors (Fig. 5b) indicate that the bottom boundary layer at the CMO site usually is well mixed in sound speed. Occasionally, however, near-bottom stratification is strong, resulting in sound-speed differences between 0.38 and 5.50 m above the bed of up to 10 m s^{-1}, which roughly corresponds to 5°C. Time series of the standard deviation of horizontal velocity $\sqrt{\sigma_u^2 + \sigma_v^2}$ (Fig. 5c) contain contributions from surface waves, internal motions, and, to a much lesser extent, turbulence. Surface waves generated by the close passage of Hurricane Edouard, a nor'easter, and Hurricane Hortense are visible as peaks in $\sqrt{\sigma_u^2 + \sigma_v^2}$ centered on days 246, 251, and 258, respectively. The intermittent peaks of short duration are associated with internal motions (often simply referred to as internal waves hereinafter) with periods on the order of 5–15 min (including trains of wavelike motions as well as more borelike features), as determined from the inspection of individual burst time series (an example of a borelike feature is presented below).

Representative spectra of longitudinal and vertical velocity fluctuations, S_{uu} and S_{ww}, during conditions of strong surface waves (Fig. 6a) contain an energetic surface-wave peak centered at 0.07 Hz, corresponding to a wavelength greater than 300 m, and a phase speed of 20 m s^{-1}. The spectral levels of the S_{uu} wave peak are more than 2 orders of magnitude larger than the underlying stress-carrying eddies. The corresponding spectrum of temperature fluctuations, S_{TT} (Fig. 6b), contains a small peak at the dominant surface-wave frequency, consistent with the estimate (3), that is, the idea that $\overline{\tilde{T}^2}/\overline{T'^2}$ is small when compared with $\overline{\tilde{u}^2}/\overline{u'^2}$.

Representative spectra of longitudinal and vertical velocity fluctuations during conditions of strong internal waves (Fig. 7a) contain a low-frequency ''hump'' in S_{uu} below 0.002 Hz. Between 0.002 and 0.01Hz, the spectral levels of the horizontal velocity fluctuations fall off rapidly, giving the spectrum an overall concave upward shape. S_{TT} also contains energetic low-frequency variability (Fig. 7b), but, in contrast to S_{uu}, the temperature spectral levels do not fall off as rapidly between 0.002 and 0.01 Hz.

b. Shear stress

It is instructive to consider the cospectra that are integrated to yield the three sets of shear stress estimates

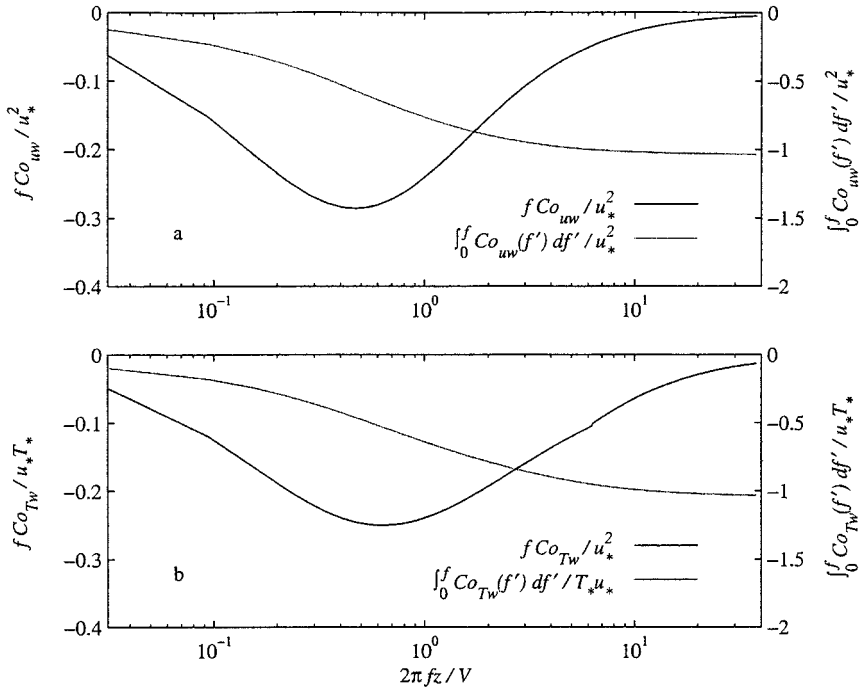

FIG. 8. Empirical energy-preserving cospectrum and running integral of cospectrum of (a) u and w and of (b) T and w as determined from measurements during neutral conditions in the atmospheric boundary layer (Kaimal et al. 1972). The cospectra are normalized by $u_* = |\overline{u'w'}|^{1/2}$ and $T_* = -\overline{T'w'}/u_*$.

described in section 3, because wave-induced contributions can be recognized as deviations from the form expected in typical boundary layer flows. For reference, we present empirical forms for Co_{uw} and the running integral of Co_{uw}, $\int_0^f \mathrm{Co}_{uw}(f')\,df'$ (known as an ogive curve) that were determined from measurements in the wall region of the atmospheric boundary layer (Kaimal et al. 1972) [and were shown to be consistent with cospectra obtained in the wall region of shallow-water, tidal-bottom boundary layers (Soulsby 1977)] in Fig. 8a. The energetic eddies responsible for transmitting stress lie approximately in the range of apparent nondimensional wavenumber $0.1 < 2\pi fz/V < 10$ with a peak near $2\pi fz/V = 1$, in which V is the burst-averaged, alongstream velocity and $2\pi f/V$ is the apparent wavenumber of the turbulent eddies advected past a point sensor by V. When energetic waves are present, this form of Taylor's hypothesis is inadequate because advection of eddies by the wave motions is important (Lumley and Terray 1983) and the actual wavenumber distribution is different than that given by $2\pi f/V$. We present the results in the form of ogive curves, which are essentially low-pass-filtered cospectra, because cospectral estimates are inherently noisy.

To illustrate the filtering process, we present an example of the estimated filter weights between elevations of 5.4 and 1.1 m above the bed [positions (2) and (1), respectively] during energetic surface-wave conditions (Fig. 9) that demonstrates that the filters are physically meaningful. For clarity, we use a notation h_{ij}, where i denotes the component of velocity that is the output of the filter and j denotes the component of velocity that is the input to the filter. The estimation of $\tilde{U}_{(1)}$ is dominated by h_{uu} (Fig. 9a), which has a maximum at zero lag, as expected for vertically separated instruments, and decreases with increasing lag, with a zero crossing near the fourth lag, or about 3.3 s, which is roughly consistent with a dominant surface-wave period of 15 s. The weights of h_{uv} and h_{uw} are near zero, indicating that $V_{(2)}$ and $W_{(2)}$ are not important inputs in the estimation of $\tilde{U}_{(1)}$, although it is reassuring that they take near-zero values. In contrast, the estimation of $\tilde{W}_{(1)}$ is not dominated completely by h_{ww} (Fig. 9b), and the weights of h_{uv} and h_{uw} are significant, with skew-symmetric peaks near the third lag, indicating that $U_{(2)}$ and $V_{(2)}$ are coherent with $\tilde{W}_{(1)}$ but are approximately in quadrature, as expected.

As an example of the effect of moderately energetic surface waves on Co_{uw}, we present a spectrum of horizontal velocity and cospectral ogive curves at 0.70 m above the bed, position (1), for a burst in which the surface-wave rms velocity equals 0.07 m s^{-1} (Fig. 10). The surface-wave spectral peak (Fig. 10a) is nearly collocated with the expected maximum in turbulence cospectral density (see Fig. 8a). The raw covariance estimate has a large contribution (visible as the region of steep slope in the ogive curve) at the frequency of the surface waves (Fig. 10b). This is anomalous for bound-

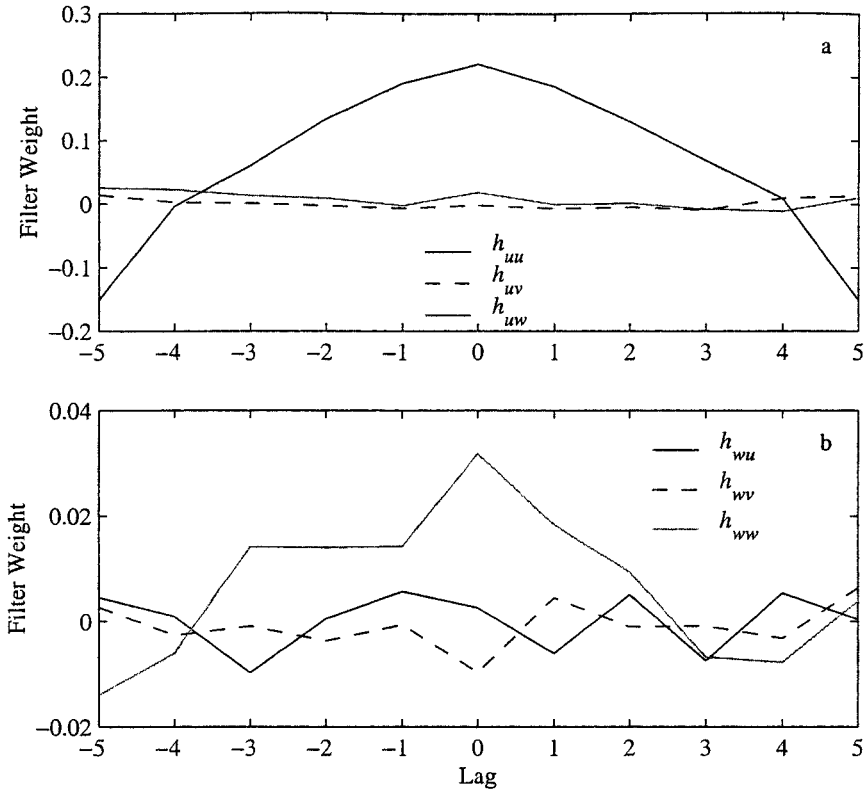

FIG. 9. Example of the filters between 5.4 and 1.1 m above the bottom: (a) h_{uu}, h_{uv}, and h_{uw} are the filter weights used to estimate $\tilde{U}_{(1)}$, given measurements of $U_{(2)}$, $V_{(2)}$, and $W_{(2)}$; (b) h_{wu}, h_{wv}, and h_{ww} are the filter weights used to estimate $\tilde{W}_{(1)}$ with the same measurements as in (a). The filter weights plotted are average values from 49 bursts when the rms surface wave velocity was greater than 0.04 m s^{-1}.

ary layer turbulence (compare with Fig. 8a) and is attributable to wave contamination. Of the two differenced estimates, cov[ΔU, $W_{(1)}$] contains little or no surface-wave contamination, while cov[$U_{(1)}$, ΔW] contains a surface-wave contribution of magnitude roughly equal to the raw estimate (Fig. 10c), consistent with expectations of section 2c. Neither of the filtered estimates, cov[$\Delta\hat{U}$, $W_{(1)}$] or cov[$U_{(1)}$, $\Delta\hat{W}$], contains a net contribution to the shear stress from surface waves (Fig. 10d). There is some contamination of $\mathrm{Co}_{U\Delta\hat{W}}$. However, the filtering has compensated in a manner that yields no net contribution to cov[$\Delta\hat{U}$, $W_{(1)}$].

As a further test of the techniques in removing surface wave contamination, we present an example of the effect on Co_{uw} of highly energetic surface waves (rms velocity equal to 0.12 m s^{-1} at 0.70 m above the bottom; (Fig. 11). As in the example for moderate surface-wave energy, the estimates cov[$U_{(1)}$, $W_{(1)}$] and cov[$U_{(1)}$, ΔW] fail to remove wave contamination (Figs. 11b,c), whereas the estimates cov[$\Delta\hat{U}$, $W_{(1)}$] and cov[$U_{(1)}$, $\Delta\hat{W}$] succeed at removing surface-wave contamination (Fig. 11d). In contrast, the differenced estimate cov[ΔU, $W_{(1)}$] also fails to remove surface-wave contamination (Fig. 11c), indicating that the filtering technique is necessary to remove wave contamination when highly energetic surface waves are present.

An example burst time series of longitudinal and vertical velocity 1.10 m above the bottom on day 253, during a period of measurable stratification (see Fig. 5b) and most likely associated with a horizontal intrusion, captures the passage of an energetic internal motion with near-bottom velocities greater than 0.1 m s^{-1} and a duration of approximately 5 min (Fig. 12a). The sound-speed record for this burst also records the passage of the ''event'' (see Fig. 15, described in next section) and indicates that the event had a borelike character. The internal motion made a large low-frequency contribution to the raw cospectrum below $2\pi fz/V = 0.02$, and although the filtered estimate is better than the raw estimate, in contrast to the case of surface waves, the proposed techniques are not successful at removing the observed wave bias (Fig. 12b). The failure is partially owing to the long duration of the internal motion as compared with the period of surface waves and the length of the burst and to the intermittent nature of the internal motion. There is also a small surface-wave bias visible in the ogive curve of $\mathrm{Co}_{\Delta\hat{U}W}$ (similar to those identified in Figs. 10 and 11), suggesting that the use

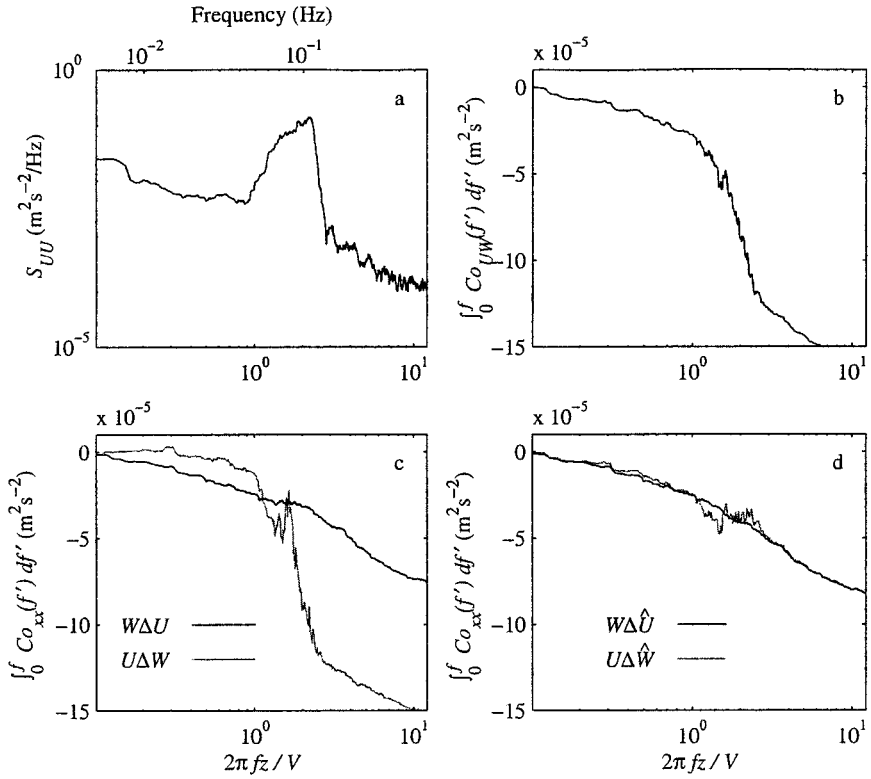

FIG. 10. Estimates of $\overline{u'w'}$ under moderately energetic surface wave conditions (surface-wave rms velocity = 0.07 m s^{-1}) from BASS measurements at 0.70 m above the bed taken on year day 246 as the energy of the surface waves forced by Hurricane Edouard diminished. (a) Energy density of longitudinal velocity fluctuations, smoothed with a 21-point boxcar filter, and ogive curves of (b) raw, (c) differenced, and (d) filtered stress estimates vs dimensionless wavenumber.

of constant filter weights during a burst with nonstationary internal wave properties degrades the ability of the filtering technique to remove surface-wave bias. In practice, the range of internal motion contamination is nearly out of the expected nondimensional wavenumber range of the energy-containing eddies (Fig. 8a) and the unwanted internal motion bias can be removed by windowing Co_{uw}.

A comparison of $\overline{u'w'}$ estimates from the entire 6-week deployment using cov($\Delta\hat{U}$, W) as a standard demonstrates that the raw shear stress estimates cov(U, W) are contaminated with surface-wave-induced covariance during the energetic surface-wave events (Fig. 13a). As anticipated in section 2c, the differenced shear stress estimate cov(ΔU, W) is mostly free of surface-wave contamination during the high-energy wave events, while cov(U, ΔW) is arguably worse than cov(U, W) (Figs. 13b,c). The two filtered estimates agree well (Fig. 13d). These results indicate that the three estimates cov(ΔU, W), cov($\Delta\hat{U}$, W), and cov(U, $\Delta\hat{W}$) are all successful at removing surface-wave bias when it exists in this dataset and that, as shown by comparison with the raw estimate, the successful techniques do not degrade the shear stress estimates when energetic surface waves are absent.

c. Heat flux

As in the case of shear stress, we consider the cospectra that are integrated to yield the three sets of $\overline{T'w'}$ estimates described in section 3, because wave-induced contributions to heat flux are also observable as deviations from the expected form of Co_{Tw} in typical boundary layer flows. Empirical forms for Co_{Tw} and the running integral of Co_{Tw}, $\int_0^f \mathrm{Co}_{uw}(f')\,df'$ (Fig. 8b) from Kaimal et al. (1972) are similar to those for shear stress, except that the range of heat-flux-carrying eddies is shifted to higher $2\pi fz/V$ in comparison with the range of stress-carrying eddies (Fig. 8a).

For the most part, the bottom boundary layer is well mixed during periods of strong surface wave activity. However, near-bottom stratification existed during Hurricane Hortense (Fig. 5b), which resulted in temperature fluctuations produced by surface waves. The stratification was inferred to result from mixed layer entrainment and was accompanied by physically meaningful buoyancy fluxes [see Shaw et al. (2001) for further discussion]. As an example of the effect of these wave-induced temperature fluctuations on Co_{Tw}, we present a temperature spectrum and cospectral ogive curves at 3.3 m above the bed, position (1) in this case, for a burst

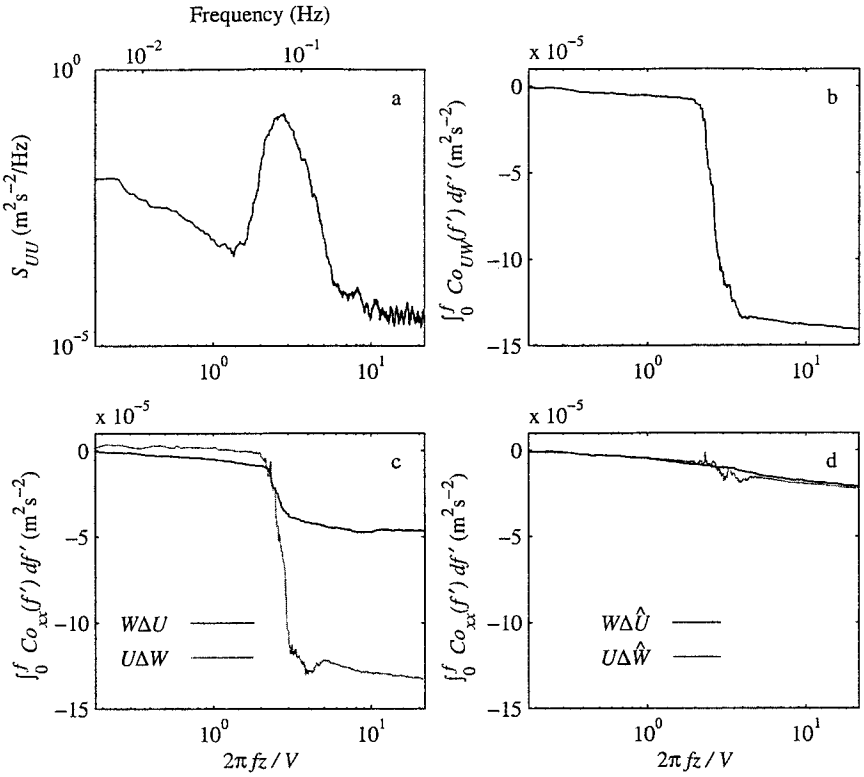

FIG. 11. Estimates of $\overline{u'w'}$ under highly energetic wave conditions (surface-wave rms velocity = 0.12 m s^{-1}) from BASS measurements at 0.70 m above the bed taken on yearday 246 as surface-wave energy forced by Hurricane Edouard peaked. (a) Energy density of longitudinal velocity fluctuations, smoothed with a 21-point boxcar filter, and ogive curves of (b) raw, (c) differenced, and (d) filtered stress estimates vs dimensionless wavenumber.

in which the rms wave-induced temperature was 0.01°C (Fig. 14). In this particular example, the surface-wave peak in the temperature spectrum (Fig. 14a) is located at the upper end of the expected range of the heat-flux-carrying eddies (Fig. 8b). The raw estimate contains an anomalous contribution at the dominant surface wave frequency (Fig. 14b). The anomaly is visible in both of the differenced estimates (Fig. 14c) and the filtered estimate cov($\Delta\hat{T}$, W) (Fig. 14d). Only in the filtered estimate cov(T, $\Delta\hat{W}$) is the observed bias removed (Fig. 14d). The heat-flux-carrying eddies in this example are located in a higher range of $2\pi fz/V$ than expected, which is probably caused by stable stratification limiting the size of eddies (compare with Fig. 8b). The pronounced effects of surface waves on estimates of heat flux contradict the theoretical scale analysis presented in section 2a.

Here, the burst containing an internal wave presented in Fig. 12 is considered in terms of the effect of the internal wave on estimates of heat flux. The time series of sound speed from 1.1 m above the bed is nearly constant until disturbed by the passage of the internal wave 16 min into the burst (Fig. 15a). The internal wave made large contributions to the raw estimate, and the contamination is not eliminated in the filtered estimate (Fig. 15b), as for the case of shear stress. In fact, both estimates result in a positive heat flux, which is countergradient for the stably stratified bottom boundary layer. Note that the sound-speed record (Fig. 15a) is inconsistent with the implicit assumption of stationarity of the statistical properties of waves within individual bursts. Unlike Co_{uw}, Co_{Tw} is contaminated well into the expected range of heat-flux-carrying eddies, above $2\pi fz/V = 1$ (Fig. 8b), so that Co_{Tw} cannot simply be windowed to remove internal wave bias without a loss of turbulent flux.

5. Discussion

The results of section 4 confirm several of the theoretical predictions of section 2. The success of the shear stress estimate $-\rho$ cov(ΔU, W) at removing surface wave bias, together with the failure of the estimate $-\rho$ cov(U, ΔW), demonstrates the importance of taking advantage of the near-bottom properties of small-amplitude, irrotational surface waves, for which $\tilde{u}$ is approximately independent of z, and $\tilde{w}$ increases linearly with z for $kz \ll 1$. The estimate $-\rho$ cov(ΔU, W) is predicted to be more effective at reducing wave bias by a factor of k^2z^2, which is approximately 10^{-4} for near-bottom

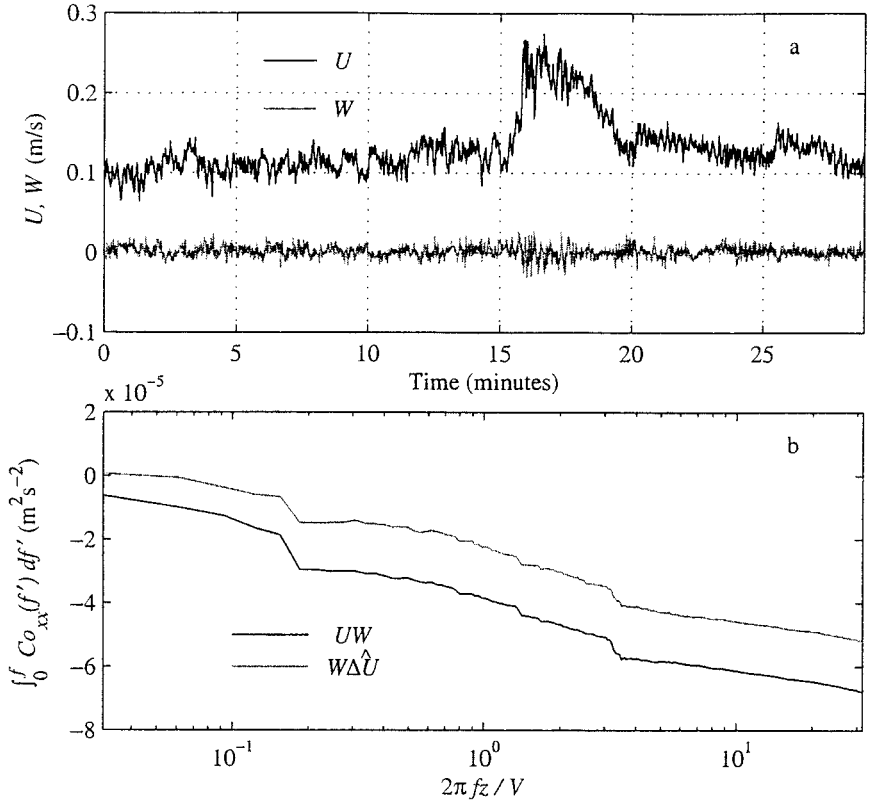

FIG. 12. Estimates of $\overline{u'w'}$ during energetic internal wave conditions from a single burst of BASS measurements 1.10 m above the bed taken on yearday 253 during a period of strong stratification. (a) Burst time series of longitudinal and vertical velocity and (b) ogive curves for cov[$U_{(1)}$, $W_{(1)}$] and cov[$\Delta\hat{U}$, $W_{(1)}$].

measurements at the CMO site with typical 15-s swell. The failure of $-\rho$ cov(ΔU, W) during energetic surface wave conditions forced by hurricane Edouard (Fig. 11c) is likely owing to either surface waves with higher than usual nonlinearity or to local flow disturbances, perhaps associated with the tripod and instrumentation, that are enhanced by larger waves. As noted in section 4, the contamination of Co_{Tw} by surface waves (Fig. 14b) is larger than expected from the estimate (4), suggesting that the estimate for wave-induced temperature fluctuations used in section 2a is not appropriate. The failure of the estimate ρc_p cov(ΔT, W) probably is caused by a lack of temperature correlation owing to a nonuniform vertical temperature gradient. The bottom at the site is smooth and fairly flat, and the surface waves are weakly nonlinear, thus the surface-wave contamination likely resulted from errors in the leveling of the instruments. The case of internal waves is more complicated and will be discussed later.

In general, the results indicate that wave bias can be reduced by accounting for spatial differences in wave-induced velocity fluctuations with empirically derived filters. In particular, the success of the estimate $-\rho$ cov(U, $\Delta\hat{W}$) (Fig. 13d) demonstrates that the filtering technique is capable of accounting for the vertical variation of w that causes the estimate $-\rho$ cov(U, ΔW) to fail (Fig. 13c). The capability of the filtering technique is further demonstrated by the success of $-\rho$ cov($\Delta\hat{U}$, W) and $-\rho$ cov(U, $\Delta\hat{W}$) when near-bottom surface wave motions were largest (Fig. 11d) and the estimate $-\rho$ cov($\Delta\hat{U}$, W) failed (Fig. 11c). For practical purposes, the filtering step is not critical for this dataset, although the results do demonstrate the potential of the filtering step in harsher wave conditions.

In practice, the adaptive filtering technique is insensitive to the exact values chosen for the number of points M in the least squares problem or the number of filter weights N, so long as $M \gg N$. A useful rule of thumb is to use a filter length such that $N\,dt$ equals a significant fraction of the wave period and to use a number of data points such that $M\,dt$ is much greater than the timescale of the largest eddies. The filtering technique requires that the turbulence is spatially incoherent at separations r, a stronger statement than requiring it to be uncorrelated. However, if turbulence is uncorrelated, it is almost certainly incoherent because eddies quickly lose their identity in turbulent flow. Including the full velocity vector in the prediction of each component of wave-induced velocity yields better stress estimates during demanding wave conditions than if only one velocity

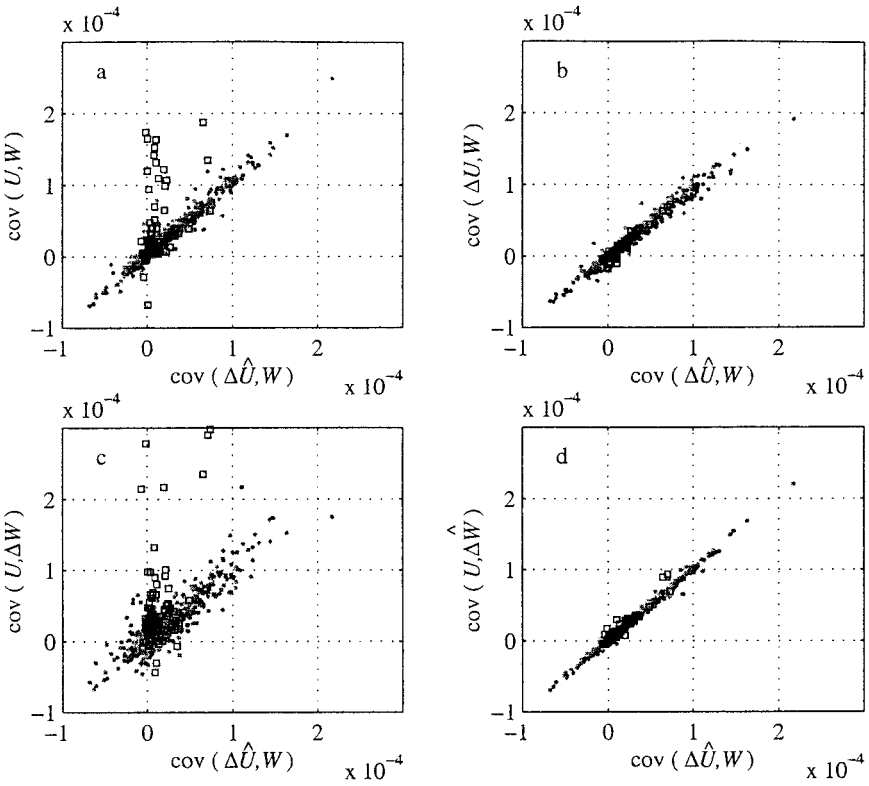

FIG. 13. Comparison of estimates of $\overline{u'w'}$ in the along-shelf direction computed from BASS measurements at 0.70 m above the bed. Here, cov($\Delta\hat{U}$, W) is taken as a standard with which the other estimates are compared: (a) cov(U, W), (b) cov(ΔU, W), (c) cov(U, ΔW), and (d) cov(U, $\Delta\hat{W}$). Bursts with surface-wave rms > 0.04 m s^{-1} are plotted as open squares. The units on all axes are meters squared per second squared.

component is used for prediction. A fully recursive filtering technique (e.g., Haykin 1996) in which the filter weights are updated continuously throughout each burst during periods of internal wave activity resulted in a loss of turbulent covariance because, on short enough timescales, large eddies can be spatially coherent.

None of the proposed techniques were completely successful at removing internal wave bias from estimates of shear stress or heat flux, although the internal wave bias for stress estimates can usually be easily removed by high-pass filtering. The differenced stress estimates most likely failed because the near-bottom variation of internal wave-induced velocity was not small, as in the case for the horizontal motions induced by surface waves. The near-bottom structure of internal-wave-induced motion is complicated by an internal-wave boundary layer height that is not small relative to the measuring heights, the slow phase speed of internal waves (which increases potential for nonlinear effects), rotational effects, and internal wave periods comparable to the length of measurement. Nonlinear effects are especially likely for internal-wave-induced temperature fluctuations because the vertical displacements caused by the passage of large internal waves are large enough to advect the density interfaces that tend to develop at the top of the mixed layer (see Fig. 15a) a considerable distance, making $\tilde{w}d\tilde{T}/dz$ large and invalidating the estimate (3). This nonlinear effect is demonstrated in the extreme example of the time series in Fig. 15a and in the spectrum and cospectrum presented in Figs. 7b and 15b for which the effect of internal waves on temperature is apparently transferred to higher frequencies. The filtered estimates fail because nonlinearity invalidates the assumptions of the linear filtration techniques and because intermittency within violates the assumption of stationary wave properties. In light of the complicated nature of the observed internal waves it is not clear how much of the internal-wave contribution to measured covariances is real or apparent. This is a question we hope to pursue in future work.

From the viewpoint of experimental design, the proposed techniques are valuable because they can be used to obtain surface-wave-free flux estimates with a vertical array of sensors, which allows the vertical structure of bottom boundary layer turbulence to be studied. In particular, the technique of differencing a single component of velocity results in a flux estimate at the height of a single sensor as opposed to an estimate that is spatially averaged. Without single differencing, it would be difficult to obtain flux estimates at a wide range of heights

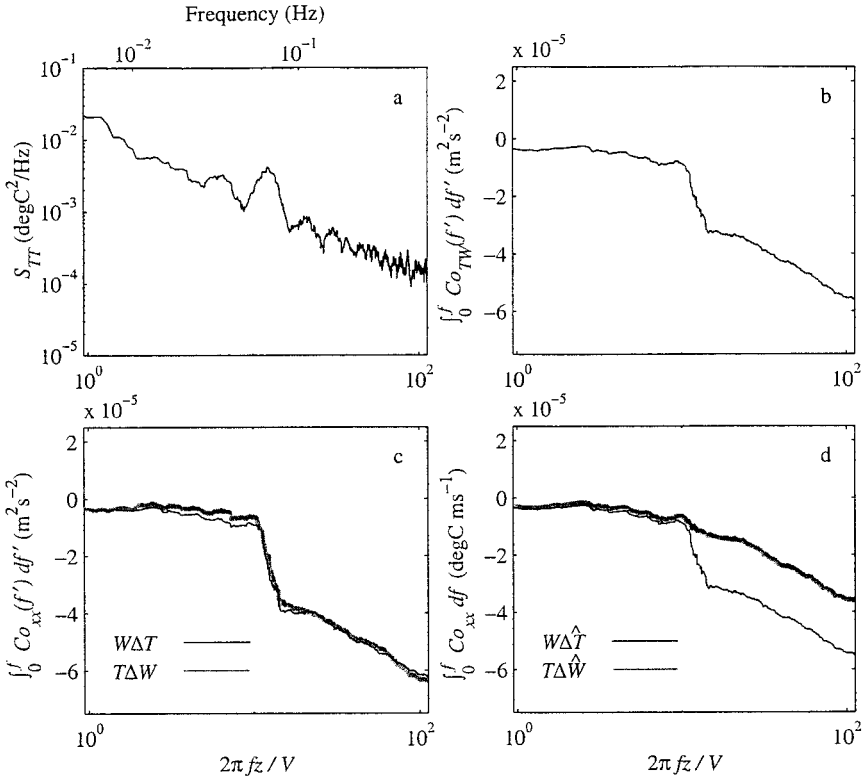

FIG. 14. Estimates of $\overline{T'w'}$ under energetic wave conditions and stratification from BASS measurements at 3.3 m above the bed taken on yearday 258 during Hurricane Hortense. (a) Energy density of temperature fluctuations, smoothed with a 21-point boxcar filter, and ogive curves of (b) raw, (c) differenced, and (d) filtered heat flux estimates vs dimensionless wavenumber.

while satisfying the condition $r > 5z$. The results presented here suggest the differenced estimate $-\rho$ cov(ΔU, W) is adequate for the removal of surface waves from stress estimates under all but the most demanding conditions on the outer shelf. For more energetic conditions, the filtered estimate $-\rho$ cov($\Delta\hat{U}$, W) can be used. To obtain surface-wave-free heat flux estimates, the estimate ρc_p cov(T, $\Delta\hat{W}$) is necessary because wave-induced temperature fluctuations are not coherent if $d\overline{T}/dz$ is strongly inhomogeneous. In practice, it is best to remove internal wave energy by high-pass filtering before the filter weights are calculated, because the presence of nonstationary internal waves can degrade the estimation of surface-wave-induced motions.

6. Summary and conclusions

This paper has presented a theoretical analysis and an oceanic test of techniques to estimate near-bottom, turbulence-induced fluxes in the presence of energetic wave motions with current meter arrays. A new adaptive filtering technique has been introduced to minimize the contributions of wave motions to measured covariances. The technique requires two sensors separated in space and requires that the coherency scale of wave motions be much larger than the coherency scale of turbulent motions. The techniques were applied to a 6-week set of coastal bottom boundary layer observations that include three energetic surface-wave events and a number of energetic internal-wave events.

Results from the oceanic test indicate the following conclusions. The proposed technique succeeds at removing surface-wave contamination from shear stress and heat flux estimates using pairs of sensors separated in the vertical dimension by a distance of approximately 5 times the height of the lower sensor, even during the close passage of hurricanes, but fails at removing longer-period, internal-motion contamination from shear stress and heat flux estimates. The presence of internal motions does not pose a significant problem for estimating turbulent shear stress because contamination caused by internal waves is limited to frequencies lower than the stress-carrying eddies. In contrast, the presence of internal motions does pose a problem for estimating turbulent heat flux because the contamination extends into the range of the heat flux–carrying eddies. The internal case is complicated by the facts that the motions are highly intermittent, the internal wave period is comparable to the period of measurement, the height of the internal wave boundary layer is on the order of the height of measurement, and, specifically for heat flux estimates, nonlinear effects are large.

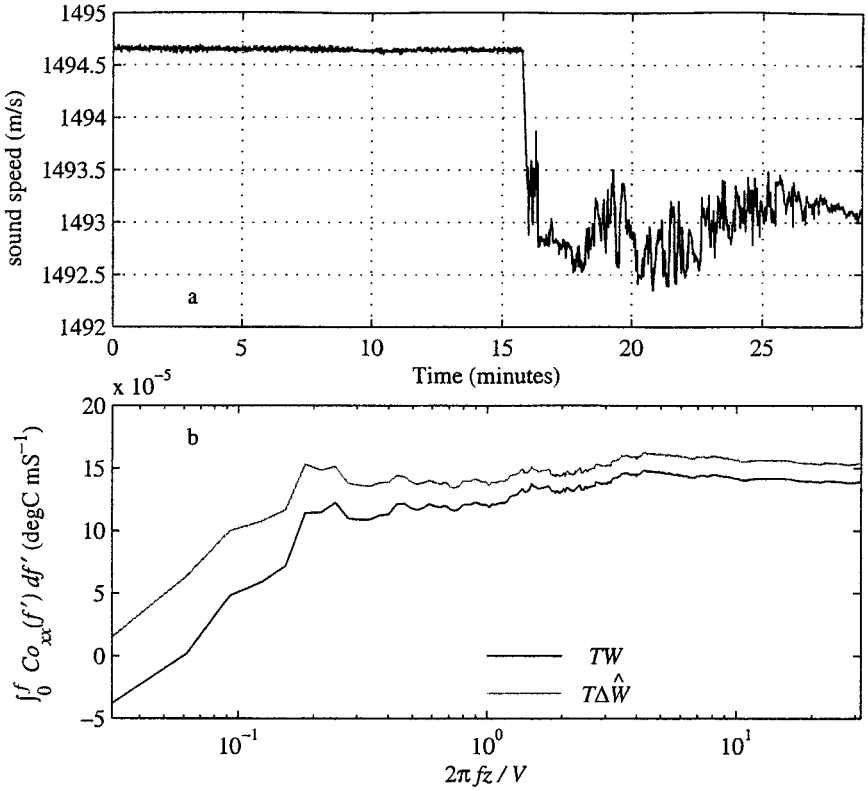

FIG. 15. Estimates under energetic internal wave conditions from a single burst of BASS measurements at 1.10 m above the bed taken on yearday 252 during a period of strong stratification. (a) Burst time series of sound speed, and (b) ogive curves for two heat flux estimates, for which the operations are performed on the vertical velocity component.

Acknowledgments. This study was supported by the Office of Naval Research under Grants N000149510373 and N000149610953. We thank James Priesig for suggesting the use of the least squares filtering method. We also thank Janet Fredericks for her preliminary processing of the data. We are grateful for the comments provided by Ole Madsen, Steve Elgar, and three anonymous reveiwers.

REFERENCES

Bowden, K. F., and L. A. Fairbairn, 1952: A determination of the frictional forces in a tidal current. *Proc. Roy. Soc. London,* **214A,** 371–391.

——, and ——, 1956: Measurements of turbulent fluctuations and Reynolds stresses in a tidal current. *Proc. Roy. Soc. London,* **237A,** 422–438.

——, ——, and P. Hughes, 1959: The distribution of shearing stresses in a tidal current. *Geophys. J. Roy. Astron. Soc.,* **2,** 288–305.

Businger, J. A., J. C. Wyngaard, Y. Izumi, and E. F. Bradley, 1971: Flux-profile relationships in the atmospheric surface layer. *J. Atmos. Sci.,* **28,** 181–189.

Charnock, H., 1959: Tidal friction from currents near the seabed. *Geophys. J. Roy. Astron. Soc.,* **2,** 215–221.

Fredericks, J. J., J. H. Trowbridge, A. J. Williams, G. Voulgaris, and W. J. Shaw, 1999: Fluid mechanical measurements within the bottom boundary layer during Coastal Mixing and Optics. WHOI Tech. Rep. 97-13, 81 pp.

Grant, W. D., and O. S. Madsen, 1986: The continental-shelf bottom boundary layer. *Annu. Rev. Fluid Mech.,* **18,** 265–305.

——, A. J. Williams, and S. M. Glenn, 1984: Bottom stress estimates and their prediction on the Northern California continental shelf during CODE-1: The importance of wave–current interaction. *J. Phys. Oceanogr.,* **14,** 506–527.

Green, M. O., and I. N. McCave, 1995: Seabed drag coefficient under tidal currents in the eastern Irish Sea. *J. Geophys. Res.,* **100,** 16 057–16 069.

Gross, T. F., and A. R. M. Nowell, 1983: Mean flow and turbulence scaling in a tidal boundary layer. *Cont. Shelf Res.,* **2,** 109–126.

——, and ——, 1985: Spectral scaling in a tidal boundary layer. *J. Phys. Oceanogr.,* **15,** 496–508.

Haykin, S., 1996: *Adaptive Filter Theory.* 3d ed. Prentice Hall, 989 pp.

Heathershaw, A. D., 1979: The turbulent structure of the bottom boundary layer in a tidal current. *Geophys. J. Roy. Astron. Soc.,* **58,** 395–430.

Huntley, D. A., and D. G. Hazen, 1988: Seabed stresses in combined wave and steady flow conditions on the Nova Scotia continental shelf: Field measurements and predictions. *J. Phys. Oceanogr.,* **18,** 347–362.

Kaimal, J. C., J. C. Wyngaard, Y. Izumi, and O. R. Cote, 1972: Spectral characteristics of surface-layer turbulence. *Quart. J. Roy. Meteor. Soc.,* **98,** 563–589.

Lueck, R. G., and Y. Lu, 1997: The logarirhmic layer in a tidal channel. *Cont. Shelf Res.,* **17,** 1785–1801.

Lumley, J. L., and E. A. Terray, 1983: Kinematics of turbulence convected by a random wave field. *J. Phys. Oceanogr.,* **13,** 2000–2007.

MacKenzie, K. V., 1981: Nine-term equation for sound speed in the oceans. *J. Acoust. Soc. Amer.,* **70,** 807–812.

Monin, A. S., and A. M. Yaglom, 1971: *Statistical Fluid Mechanics.* MIT Press, 769 pp.

Pond, S., 1968: Some effects of buoy motion on measurements of wind speed and stress. *J. Geophys. Res.,* **73,** 507–512.

Shaw, W. J., A. J. Williams, and J. H. Trowbridge, 1996: Measurement of turbulent sound speed fluctuations with an acoustic current meter. *Proc. Oceans 96,* Ft. Landerdale, FL, MTS/IEEE, 105–110.

——, J. H. Trowbridge, and A. J. Williams, 2001: The budgets of turbulent kinetic energy and scalar variance in the continental shelf bottom boundary layer. *J. Geophys. Res.,* **106,** 9551–9564.

Soulsby, R. L., 1977: Similarity scaling of turbulence spectra in marine and atmospheric boundary layers. *J. Phys. Oceanogr.,* **7,** 934–937.

Sternberg, R. W., 1968: Friction factors in tidal channels with differing bed roughness. *Mar. Geol.,* **6,** 243–260.

Tennekes, H., and J. L. Lumley, 1972: *A First Course in Turbulence.* MIT Press, 300 pp.

Trivett, D. A., 1991: Diffuse flow from hydrothermal vents. Ph.D. thesis, WHOI/MIT, 216 pp.

Trowbridge, J. H., 1998: On a technique for measurement of turbulent shear stress in the presence of surface waves. *J. Atmos. Oceanic Technol.,* **15,** 290–298.

——, W. R. Geyer, M. M. Bowen, and A. J. Williams, 1999: Near-bottom turbulence measurements in a partially mixed estuary: Turbulent energy balance, velocity structure, and along-channel momentum balance. *J. Phys. Oceanogr.,* **29,** 3056–3072.

Williams, A. J., J. S. Tochko, R. L. Koehler, W. D. Grant, T. F. Gross, and C. V. R. Dunn, 1987: Measurement of turbulence in the oceanic bottom boundary layer with an acoustic current meter array. *J. Atmos. Oceanic Technol.,* **4,** 312–327.